IEEE Journal of Microwaves

Received 3 July 2023; revised 26 July 2023; accepted 18 August 2023. Date of publication 25 August 2023; date of current version 9 October 2023.

Digital Object Identifier 10.1109/JMW.2023.3307297

A Low-Insertion Loss Cryogenic Edge-Mode Isolator With 18 GHz Bandwidth

LINGZHEN ZENG, CHEUK-YU EDWARD TONG (Member, IEEE), AND SCOTT N. PAINE

(Regular Paper)

Center for Astrophysics - Harvard and Smithsonian, Cambridge, MA 02138-1516 USA

CORRESPONDING AUTHOR: Lingzhen Zeng (e-mail: lingzhen.zeng@cfa.harvard.edu).

This work was supported by FY2023 North American (NA) ALMA Development Study under Grant 1519126.

ABSTRACT Cryogenic isolators play an important role in low-noise receiver systems widely employed in millimeter and submillimeter telescopes. To enable a significantly wider Intermediate Frequency (IF) bandwidth, there is strong demand for a wideband, low-loss isolator in modern facilities like the Submillimeter Array (SMA) and Atacama Large Millimeter/submillimeter Array (ALMA). In this article, we present a novel cryogenic edge-mode isolator that incorporates an innovative circuit design. Operating at a cryogenic temperature of 4 K, this isolator delivers unprecedented performance, covering a frequency range from 4 GHz to 22 GHz. It exhibits insertion loss of less than 1 dB, together with return loss below -15 dB. In particular, it provides an isolation better than 17 dB across most of the band, a significant improvement over the previous generation of edge-mode isolators. This new isolator design is suitable for a wide array of low-noise receiver applications, from radio-astronomy to quantum computing.

INDEX TERMS Calcium vanadium, ferrite devices, isolators, millimeter wave and terahertz components, quantum computing, radio astronomy, YIG.

I. INTRODUCTION

Low-noise receiver systems are widely used in radio astronomy, remote sensing, and various other applications. These systems typically involve heterodyne mixers or multiplexed detectors, which are followed by a cryogenic low-noise amplifier (LNA). However, there are often impedance mismatch issues between the mixer or detector and the LNA, leading to undesirable effects such as instabilities and standing waves caused by reflections. To mitigate the impact of these reflections, a common approach is to incorporate an isolator between the mixer/detector and the LNA.

In the millimeter/submillimeter waveband, advanced facilities such as the Submillimeter Array (SMA) and the Atacama Large Millimeter/submillimeter Array (ALMA) make use of state-of-the-art superconductor-insulator-superconductor (SIS) heterodyne mixers. These advanced mixers offer an exceptionally wide Intermediate Frequency (IF) bandwidth that spans two or more octaves [1], [2], [3], [4], [5]. Consequently, there is strong demand for a wideband cryogenic isolator capable of providing low insertion loss and high isolation across this broad frequency range.

Conventional Y-junction isolators are typically limited to providing useful bandwidth of approximately one octave, making them unsuitable for ultrawideband applications. An alternative design is the edge-mode isolator (also known as edge-guide mode isolator), which was proposed by Hines [6]. This design is based on the edge mode effect of the electromagnetic wave as it propagates along a stripline inside a ferrite substrate under a DC magnetic bias. By asymmetrically loading the guide edges, nonreciprocal behavior can be achieved. Hines's original isolator design has undergone significant development and improvement by various groups [7], [8], [9], [10]. The bandwidth performance of the edge-mode isolator has been extensively investigated by Courtois et al. [7] and Forterre et al. [8]. There now exist commercial edge-mode isolators which offer operating bandwidths that can approach two octaves. Several ALMA receiver bands employ cryogenic isolators which cover 4 to 12 GHz [11], [12].

We have previously reported an optimized edge-mode isolator [13] for cryogenic operations, which features a refined circuit geometry with a robust mechanical layout. This isolator demonstrates a low insertion loss of less than 1 dB, with

This work is licensed under a Creative Commons Attribution 4.0 License. For more information, see https://creativecommons.org/licenses/by/4.0/

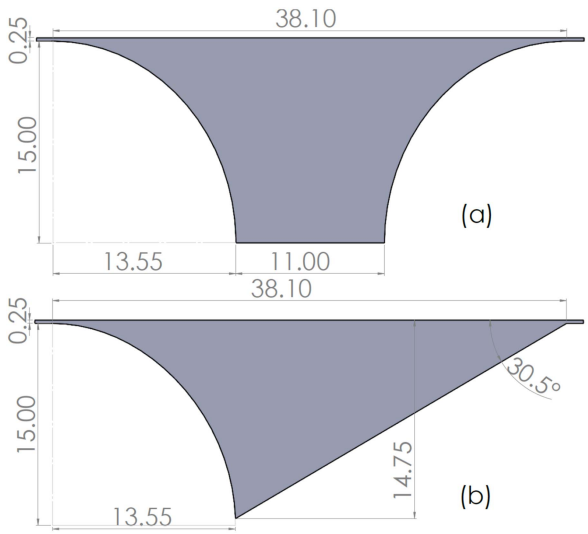

FIGURE 1. Drawings of the conventional symmetric isolator circuit from [13] (a) and the new asymmetric circuit (b). The units are in millimeters. On the input side (left), both circuits are identical. On the output side (right), the taper has been replaced by a straight one with an angle $\delta = 30.5°$ in relation to the other edge.

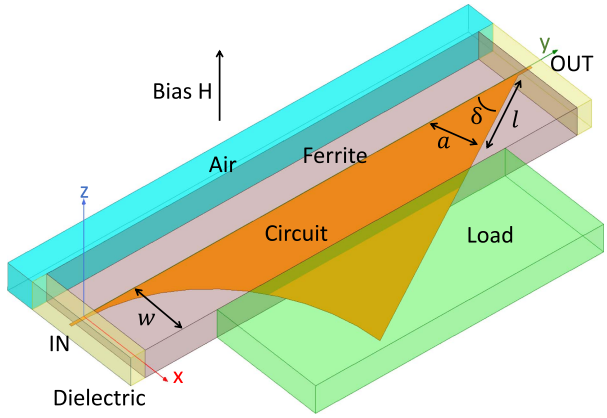

FIGURE 2. 3D model of our new edge-mode cryogenic isolator. An asymmetric copper stripline is sandwiched between two ferrite substrates and two load absorbers. External bias magnetic field is applied along the z-axis. The incident wave propagates along the straight edge of the circuit in the direction of the positive y-axis. The reverse wave excited at the output port propagates along the opposite edge and is absorbed by the load absorbers.

excellent impedance matching from 4 to 22 GHz, and notable isolation below 13 GHz. However, at higher frequencies, the measured isolation was only approximately 10 dB with correspondingly limited ability to reduce strong reflections between the mixer/detector and the LNA.

In this article, we report on the design, fabrication, and measurement of a new edge-mode isolator. The key feature of this design is an asymmetric circuit geometry that effectively reduces the excitation of unwanted ferrite volume modes in the reverse propagation waves, thus improving its reverse isolation performance. Using this design, we have demonstrated an enhanced reverse isolation, of better than 17 dB across the majority of the 4 to 22 GHz band, while maintaining similar insertion loss and return loss characteristics to those presented in [13].

The rest of this article is organized as follows. In Section II, we provide a detailed explanation of the basic theory and the initial guess values employed in our isolator design. Section III shows the simulation results, comparing the reflective wave propagation between conventional circuits and our novel design. In Section IV, we present the fabrication process of our prototype isolator as well as corresponding measurement results. The measurement and simulation results are compared in Section V. This section also compares the performance of the new isolator to the previous design presented in [13]. Finally, in Section VI, we discuss the potential applications and future developments of this edge-mode isolator.

II. EDGE-MODE ISOLATOR ANALYSIS

Fig. 1(a) shows a conventional symmetric edge-mode isolator circuit design commonly found in the literature [6], [7], [8], [9], [10], [13]. This design achieves good impedance matching at both ports through carefully optimized transition tapers. However, as shown in Section II-B, the reverse wave traveling along the concave taper edge on the right-hand side can excite higher order volume modes into the ferrite [14]. These modes can freely propagate from the output port to the input port without being absorbed by the loads, resulting in poor isolation performance. Moreover, as the frequency increases and the radius of curvature of the taper decreases, more energy is excited into these volume modes. To address this issue, we have adopted an asymmetric circuit design in which the reverse wave also propagates along a straight edge, like the forward wave. The circuit design is illustrated in Fig. 1(b).

A 3D model of our new edge-mode isolator using this asymmetric circuit is shown in Fig. 2. The basic layout comprises an asymmetric stripline circuit design with ferrite substrates plus a load absorber. Under the effect of the external DC bias magnetic field, the incident electromagnetic wave propagates along the top straight edge, from the input port to the output port with minimal insertion loss. Meanwhile, the reverse wave from the output port travels along the opposite straight edge and is effectively absorbed by the loads, yielding a high level of isolation between the two ports.

A. FORWARD WAVE PROPAGATION

As shown in Fig. 2, the ferrite slabs are much wider than their thickness. Consequently, only a small fraction of the RF energy will be present in the fringing fields outside the slabs. By ignoring the effect of the fringing fields, the isolator structure may be consider as electromagnetically closed. We can assume a perfect magnetic wall boundary condition at the edge of $x = 0$, that is $H_y = 0$. Using this boundary condition, Hines [6] found that edge-modes associated with a straight conduction line with very large or semi-infinite width are

transverse electromagnetic (TEM) modes. With the coordinates defined in Fig. 2 and assuming that the field at the edge is E_0, the fields of these calculated modes exhibit a spatial dependence term given by:

$$E_z = E_0 \exp(-\alpha_x x)\exp(-j\beta_y y), \tag{1}$$

where

$$\beta_y = \omega\sqrt{\epsilon_0\mu_0\epsilon_f\mu_1} \tag{2}$$

$$\alpha_x = \frac{\mu_2}{\mu_1}\beta_y. \tag{3}$$

Here ω is the operating frequency, ϵ_0 and μ_0 are the dielectric permittivity and magnetic permeability in vacuum, respectively, ϵ_f is the relative dielectric permittivity of the ferrite, μ_1 and μ_2 correspond to the diagonal and off-diagonal elements, respectively, of the permeability tensor associated with the ferrite. They can be expressed as

$$\mu_1 = 1 + \frac{\omega_0\omega_m}{\omega_0^2 - \omega^2} \tag{4}$$

$$\mu_2 = \frac{\omega\omega_m}{\omega_0^2 - \omega^2}, \tag{5}$$

where ω_0 is the ferromagnetic resonance frequency proportional to the internal magnetic field in the ferrite, and ω_m is the saturation magnetization frequency of the ferrite,

$$\omega_0 = -\gamma_0 H_i \tag{6}$$

$$\omega_m = -\gamma_0 M_s. \tag{7}$$

Here γ_0 is the gyromagnetic ratio, H_i is the internal magnetic field and M_s is the saturation magnetization of the ferrite material. In conventional units, H_i is typically measured in Oersted (Oe), and the saturation magnetization of the ferrite ($4\pi M_s$) is measured in gauss, so that $\gamma_0/(2\pi)$ is approximately 2.80 MHz/Oe.

An edge-mode isolator is commonly biased to have a weak internal field. Specifically, the external field is set to be $H = M_s/3$ to achieve optimal bandwidth performance [8]. Under this biasing condition, the internal field within the ferrite is considered to be negligible. By assuming $\omega_0 = 0$, the above equations can be simplified as the following

$$\mu_1 = 1 \tag{8}$$

$$\mu_2 = \frac{\omega_m}{\omega} \tag{9}$$

$$\beta_y = \omega\sqrt{\epsilon_0\mu_0\epsilon_f} \tag{10}$$

$$\alpha_x = \omega_m\sqrt{\epsilon_0\mu_0\epsilon_f}, \tag{11}$$

The Trans-Tech TTVG-1100 used in our isolator has $\epsilon_f = 14.1$ and $4\pi M_s = 1100$ G at room temperature, the corresponding saturation magnetization frequency is $f_m = \omega_m/(2\pi) = 3.1$ GHz. At a cryogenic temperature of 4 K, the saturation magnetization value increases [13], leading to a f_m value of approximately 6.0 GHz. The scale length of the electric field is calculated to be $\alpha_x \approx 0.5$ mm^{-1}, which remains constant across the entire operation band.

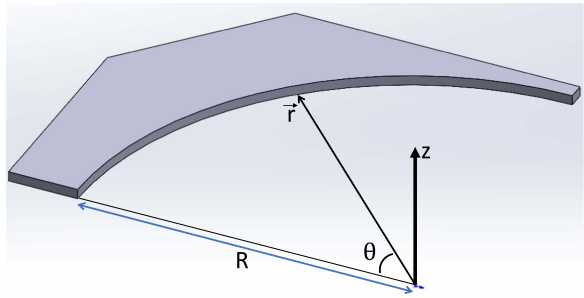

FIGURE 3. The cylindrical coordinates defined for analyzing a concave taper with a constant radius of curvature of R.

Referring to Fig. 2, the knowledge of α_x allows us to put an initial guess on the position of the absorptive load, w, with respect to the top edge of the isolator circuit. Assuming that power is absorbed beyond $x > w$, we can calculate the value of for 1 dB insertion loss ($w_{1\,\mathrm{dB}}$) in the fundamental edge-mode using this equation,

$$\frac{\int_{w_{1\,\mathrm{dB}}}^{\infty} E_z^2 dx}{\int_0^{\infty} E_z^2 dx} = \frac{\int_{w_{1\,\mathrm{dB}}}^{\infty} \exp(-2\alpha_x x)dx}{\int_0^{\infty} \exp(-2\alpha_x x)dx} = 1\ \mathrm{dB}. \tag{12}$$

The calculated value of $w_{1\,\mathrm{dB}}$ is approximately 2 mm, which is the width of a lossless stripline under pure edge-mode with a perfect load. However, in practice, various other losses are present, including dielectric, magnetic, and conduction losses within the stripline, as well as power loss in the fringing field. Additionally, significant losses occur at the transitions between the SMA connectors and the stripline. The width of the stripline needs to be significantly larger than $w_{1\,\mathrm{dB}}$ to compensate for these losses. As a first approximation, We use a initial guess of $w = 4w_{1\,\mathrm{dB}} = 8$ mm to minimize the total insertion loss.

B. REVERSE WAVE PROPAGATION

While the forward edge-mode wave propagates along a straight edge, we now examine the two designs, as illustrated in Fig. 1, in which the reverse edge-mode propagates along two different edge types.

1) CONCAVE TAPER

No simple analytic solution exists for the electromagnetic fields associated with arbitrary tapers. As an approximation, De Santis [14] analyzed the fields of the edge-mode waves over a concave edge with a constant radius of curvature using cylindrical coordinates. We present a summary of the findings in this section.

Following the cylindrical coordinates as defined in Fig. 3 and assuming that the electromagnetic field is a superposition of pure TM modes, the wave equation can be expressed as follows:

$$[\nabla_{r,\theta}^2 + K_f^2]E_z(r,\theta) = 0, \tag{13}$$

with

$$K_f = \omega\sqrt{\epsilon_0\mu_0\epsilon_f\mu_{\text{eq}}} \tag{14}$$

$$\mu_{\text{eq}} = \frac{\mu_1^2 - \mu_2^2}{\mu_1}. \tag{15}$$

A simple solution for this wave equation is

$$E_z(r,\theta) = E_0 \text{H}_n^{(2)}(K_f r)e^{\pm jn\theta}, \tag{16}$$

where $\text{H}_n^{(2)}$ is a Hankel function of the second kind, and n is the azimuth index. Similar to the case of a straight edge, we can assume a perfect magnetic wall boundary condition at $r = R$ and derive the characteristic equation for this solution as follows:

$$K_f R \frac{\text{H}_n^{(2)\prime}(K_f R)}{\text{H}_n^{(2)}(K_f R)} = \pm n\frac{\mu_2}{\mu_1}. \tag{17}$$

In weakly biased edge-mode isolators ($\omega_0 = 0$), at high frequencies where $\omega \gg \omega_m$, the equivalent permeability μ_{eq} is greater than 0, resulting in a real and positive value for $K_f R$. Under these conditions, (17) can be solved for n. It is found that n becomes a complex quantity $n = n_1 + jn_2$ with $n_1^2 \gg n_2^2 > 0$, indicating that radiation occurs in the radial direction into the ferrite volume at $r > R$. The wave is propagating in a leaky edge-mode. De Santis [14] also discovered that as the curvature of the edge increases ($R \to 0$), the amount of the leakage also increases. To minimize the leakage into the volume modes, it is necessary to set $R = \infty$, which means changing the concave taper to a linear one.

2) LINEAR TAPER

As shown in Fig. 2, for a fixed angle δ between the two straight edges, the width of the stripline, denoted as a, at a distance l from the output port is simply $a = l\tan(\delta)$. For a stripline with a finite width of a, the electromagnetic solution consists of multiple TE_n modes. Here n is the number of the E-field nulls underneath the stripline width. It is important to note that these modes are different from the volume modes discussed in the previous section. Among these TE modes, TE_0 is the fundamental mode, characterized by an exponential field distribution as a function of x (edge-mode). For the higher order modes, the fields exhibit sinusoidal variations along x. By assuming perfect magnetic wall boundary conditions at $x = 0$ and $x = \text{a}$, Hines [6] determined that:

$$\beta_y = \sqrt{\omega^2\epsilon_0\mu_0\epsilon_f\mu_{\text{eq}} - (n\pi/a)^2}. \tag{18}$$

As mentioned previously, in edge-mode isolators, μ_{eq} is typically greater than 0. The TE_n mode can propagate if the following condition is met:

$$a > \frac{n\pi}{\sqrt{\omega^2\epsilon_0\mu_0\epsilon_f\mu_{\text{eq}}}} = na_0, \tag{19}$$

where a_0 represents the characteristic width of the stripline. For our specific isolator, a_0 is calculated to be approximately 2 mm at 20 GHz. If $a > a_0$, the first order TE_1 mode can propagate. As the reverse wave travels along the straight edge from the output port, the value of a increases, allowing for the propagation of higher-order TE modes. Theoretically, the best isolation can be achieved if we use a very narrow circuit and place the load very close to its edge, where $w < a_0$, allowing only the fundamental TE_0 mode to propagate. However, as explained in Section II-A, w needs to be a few times larger than $w_{1\,\text{dB}}$ to minimize the insertion loss. Clearly, a trade-off is necessary. According to Hines [6], as $a \to \infty$, the continuum of TE modes propagating along the stripline converges to a TEM mode, which has been discussed in Section II-A. Under this condition, the power of the reverse wave will concentrate along the straight edge of the circuit and can easily be absorbed by the load.

In order to improve the isolation performance for a large value of w, one can increase the value of δ, which allows the width (a) to increase more rapidly, approaching the semi-infinite condition described above. This transformation converts the circuit from a finite-width stripline to a semi-infinite line. However, a larger δ results in poorer impedance matching at the output port due to the dramatic change in the stripline width. Therefore, optimization is necessary to strike a balance between isolation and return loss performance at the output port. As an initial guess, we set δ to 45°. This choice means that at the edge of the load, where $w = 4w_{1\,\text{dB}} \approx 8$ mm, $a \approx 11$ mm, which is considerably larger than a_0 at 20 GHz. Another approach to consider is extending the length of the circuit, allowing for a large enough stripline width (a) for a given w using a smaller δ angle. This approach can improve the S_{22} performance; however, the insertion loss will be higher due to the longer circuit, and the isolator takes up more volume.

III. ISOLATOR SIMULATION AND OPTIMIZATION

Similar to our previous work described in [13], the new isolator is simulated using the Ansys Electronics Desktop (AEDT) simulator. Fig. 2 illustrates the final 3D model after several optimization iterations. Dielectric spacers, with a dielectric constant of $\epsilon_r = 14.1$, are placed between the ferrite substrate and the input and output ports, because the simulator does not support excitation ports in direct contact with the ferrite material. In our prototype isolator, as described in Section IV, the excitation ports and dielectric spacers have been replaced with a pair of 2.92-mm SMA microwave connectors.

The ferrite material used in this isolator design is the TTVG-1100 narrow-linewidth calcium vanadium doped garnet from Trans-Tech, Inc. The thickness of the ferrite substrate is 1.0 mm. Based on the studies conducted in [13], the saturation magnetization ($4\pi M_s$) of this ferrite material shifts from 1100 G at room temperature to approximately 2130 G at 4 K temperature. For simulations, we employed the $4\pi M_s$ value at 4 K. However, due to the lack of measurement data at cryogenic temperatures, we still adopted the room temperature values provided by the ferrite vendor for the dielectric constant and loss tangent. The load material used is the Eccosorb MF-116 magnetically loaded epoxy stock from Laird

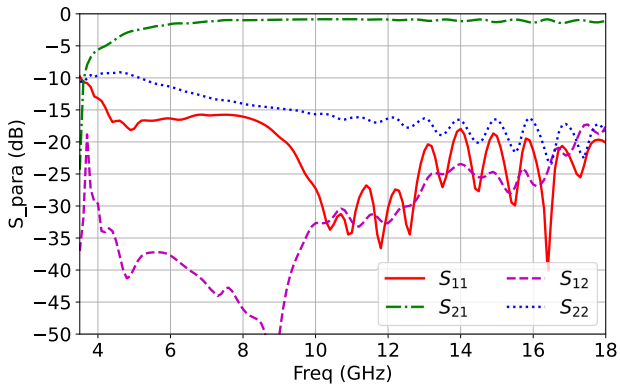

FIGURE 4. Simulated S-parameters of our edge-mode isolator with asymmetric circuit.

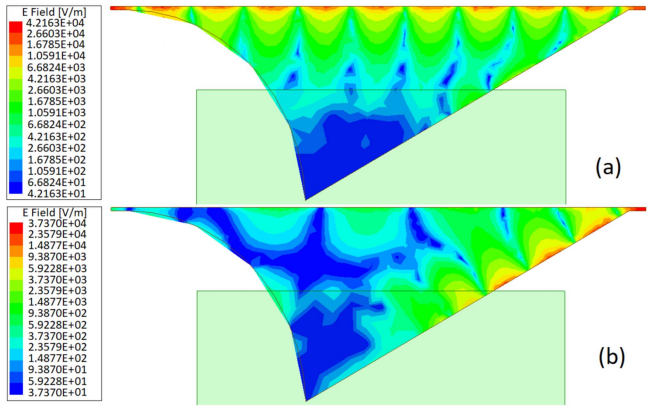

FIGURE 5. Simulated electric field distribution at 10 GHz superimposed on the circuit and load geometry. (a) illustrates the incident wave propagating from the input port (left) to the output port (right) with an input power of 1 W. (b) shows the reverse wave traveling from the output port into the load with the same power of 1 W.

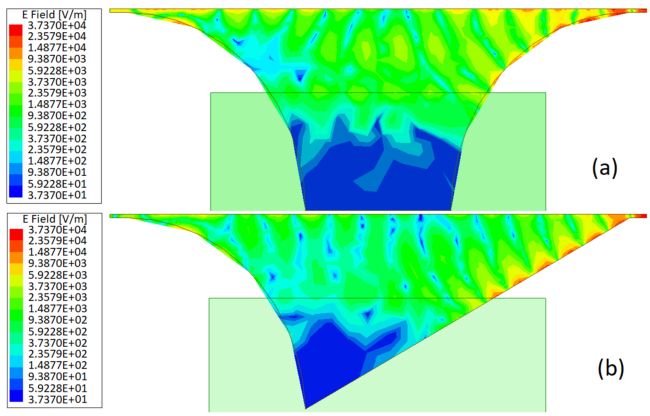

FIGURE 6. Simulated electric fields for the reverse wave at 18 GHz comparing a conventional circuit (a) (from [13]) and the new asymmetric circuit (b). With an equal excitation power of 1 W, the new isolator excites significantly lower power excitation into the volume mode, resulting in a substantial improvement in isolation performance.

Technologies. Here again, we could only find electromagnetic properties of MF-116 up to 18 GHz at room temperature. Additionally, in AEDT simulations, the DC magnetic bias in the ferrite needs to be set to achieve full saturation, resulting in a strongly biased scenario. We assumed that the external bias is equal to the saturation magnetization of the ferrite to minimize the internal field.

Due to the limitations in the simulations mentioned above, we anticipate some degree of discrepancy between the simulation and prototyping measurement results. Nevertheless, it is important to emphasize that the observed discrepancies are not substantial, and the simulations offer valuable guidance throughout the prototyping process. In this work, our design goal was to achieve an insertion loss of less than 1.0 dB, a return loss level better than −15 dB, and an isolation higher than 15 dB across the band from 4 GHz to 22 GHz. To achieve these specifications, we conducted multiple iterations of simulation and prototyping.

During the optimization process, we kept the length of the circuit and the input taper fixed, as they had been previously optimized [13]. With initial guess values of $w = 8$ mm and $\delta = 45^\circ$ (refer to Section II for details), we constructed a penalty function to determine the optimal values for w and δ that would strike a balance between the return loss at the output port (S_{22}) and the isolation performance ($|S_{12}|$). Subsequently, we fabricated the first set of prototypes and compared the measurement results at cryogenic temperatures with the simulation results. The observed discrepancies between them were taken into account for subsequent rounds of simulation and prototyping. After several iterations, we achieved a final design with measurement results meeting the design goals. The final circuit dimensions are given in Fig. 1(b), wherein the optimal values of w and δ were determined to be 6.5 mm and 30.5°, respectively. The simulated S-parameters of our final design are shown in Fig. 4.

Fig. 5 illustrates the electric field distributions at 10 GHz obtained from the simulations for both the incident and reverse waves. The principle of the edge-mode isolators can be observed, where the electric field of the forward propagating wave aligns with the top edge of the circuit (a), while the reverse wave follows the other edge and is absorbed by the load (b). As anticipated in Section II-A, the propagation constants for both waves are identical.

To demonstrate the advantage of the asymmetric circuit design, we compare the electric field of the reverse wave in the previous design from [13] with the results from this work. Fig. 6 shows the electric fields at 18 GHz for both designs, where the volume modes become significant. The electric fields are plotted under the same color scale for direct comparison. It is evident that the power in the volume modes, which can freely propagate in the ferrite substrate, is considerably lower in the new isolator. This substantial reduction in power results in a significant improvement in the isolation performance.

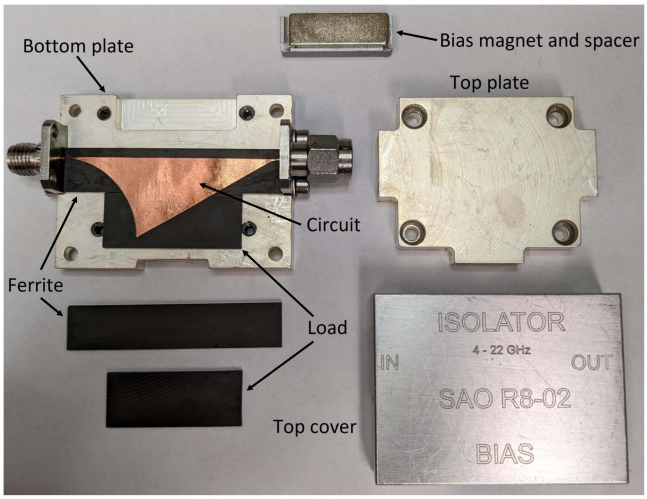

FIGURE 7. A photo of prototype isolator components. This is a stripline design with 1.0 mm thick top and bottom ferrite substrates. The magnet provides the external DC magnetic bias. The drawing of the asymmetric copper circuit is shown in Fig. 1(b).

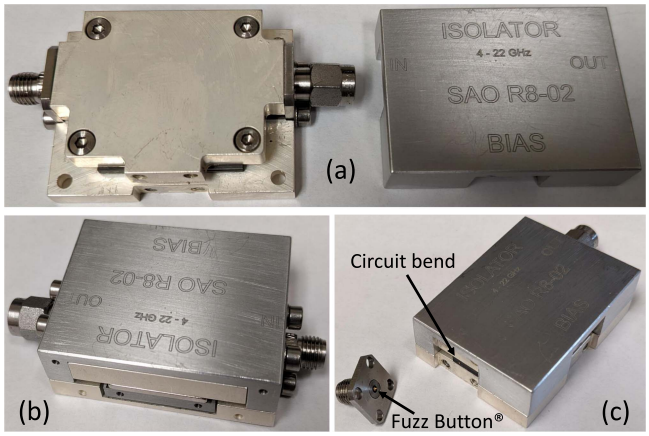

FIGURE 8. Photos of the final prototype assemblies. (a) shows the main assembly and the top cover. The full assembly is shown in (b). (c) shows the Fuzz Button pins and the circuit bend over the ferrite edge.

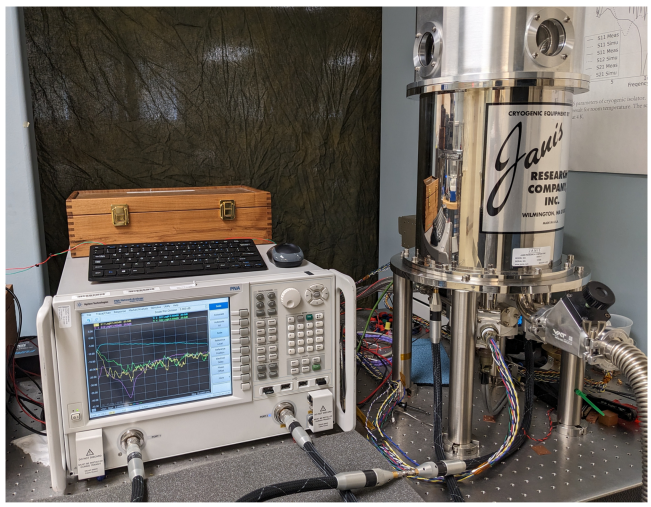

FIGURE 9. A photo of the cryogenic measurement setup used for testing prototype isolators. (The traces shown on the VNA screen are the raw data at room temperature before calibration.)

IV. ISOLATOR FABRICATION AND MEASUREMENT

We utilized an isolator prototype design that is similar to the one presented in [13]. The components of the final prototype isolator are shown in Fig. 7. The device is a stripline design consisting of a 25 μm thick copper circuit and 1.0 mm thick ferrite substrates. The specific details of the asymmetric copper circuit can be found in Fig. 1(b). A neodymium magnet block with a spacer inserted from the top of the isolator provides the bias magnetic field. Our measurements confirm that this neodymium magnet offers a stable field across a range of temperatures, from room temperature to cryogenic conditions. The magnetic field is tuned to approximately $H \approx M_s/3$. The top and bottom plates are made from 1018 low carbon steel, coated with 3-μm-thick silver layers to enhance electrical conductivity. Furthermore, an aluminum cover is installed over the top plate to protect the internal components of the isolator.

Fig. 8(a) displays the final prototype with the top protective cover removed, while Fig. 8(b) shows the complete assembly. The overall dimensions of the assembly without the SMA connectors are approximately 44 mm $\times$ 33 mm $\times$ 15 mm. The magnet block can be easily installed and removed with a spacer, using two screws inserted in the taped holes in the spacer as a handle. As the ferrite substrates, steel plates, and copper circuit have distinct coefficients of thermal expansion (CTEs), maintaining a reliable RF contact between the SMA connectors and the circuit over multiple thermal cycles poses a challenge. To address this issue, we utilized Fuzz Button contact pins from Custom Interconnects, as illustrated in Fig. 8(c). The center pins in the SMA connectors are replaced by Fuzz Button contact pins, which protrude from the center of the connectors and make contact with small bends in the copper circuits over the ferrite edges. This technique of soft contact is inherited from our previous work presented in [13] and has been demonstrated to be a reliable solution that withstands repeated thermal cycles.

The prototype isolators were measured at a cryogenic temperature of 4 K using a closed–cycle cryostat and a PNA N5224 A vector network analyzer (VNA) manufactured by Agilent Technologies. The measurement setup can be seen in Fig. 9. The VNA provides a wide bandwidth ranging from 10 MHz to 43.5 GHz, while the cryostat maintains a base operating temperature of approximately 3.2 K and incorporates temperature regulation through PID control. Cryogenic coaxial cable pairs are installed from the bottom 300 K stage to the 4 K plate in the cryostat. The measurement procedure for the isolators was conducted as follows: During the initial cooldown, we conducted a reference measurement by connecting the pair of coaxial cables at the 4 K stage, forming a closed loop. Subsequently, in the second cooldown,

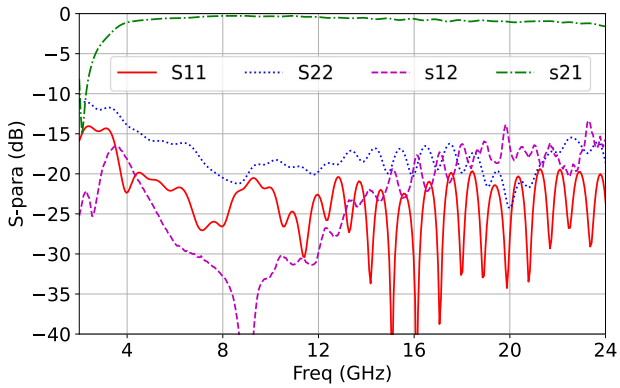

FIGURE 10. **The S-parameters of our final isolator prototype from 4 K cryogenic measurements.**

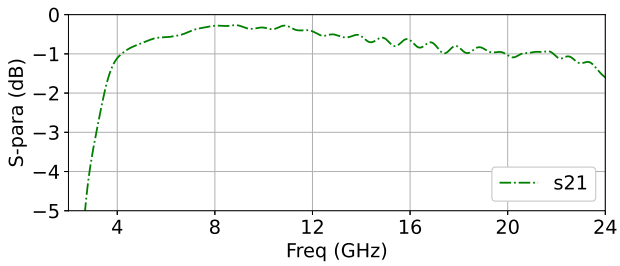

FIGURE 11. **A zoomed-in view of the measured insertion loss from Fig. 10.**

we obtained the measurement data by inserting the Device Under Test (DUT) between the same pair of coaxial cables. Finally, we de-embedded the DUT data using a process that involved dividing the measurement data by the reference data and implementing time domain gating. We have shown that this calibration technique gives consistent result and achieves an accuracy level of ∼0.05 dB for the insertion loss measurements at 4 K.

The measured S-parameters for the asymmetric isolator prototype at a temperature of 4 K are presented in Figs. 10, and 11 gives a more detailed plot for S_{21}. This isolator demonstrates good input return loss (S_{11}) better than −15 dB, mostly below −20 dB across the entire 4 to 24 GHz frequency range. The output return loss (S_{22}), is somewhat higher due to the asymmetric circuit design, but it still maintains performance better than −15 dB throughout most of the operating band. The isolation ($|S_{12}|$) is better than 17 dB across the majority of the frequency band. This is a significant improvement over the symmetrical isolator design, which only provides around 10 dB of isolation for frequencies above 16 GHz [13]. As for the insertion loss, it remains below 1.0 dB for most of the band, spanning from 4 to 22 GHz, which is comparable to the symmetrical isolator design. These measurement data confirm the excellent performance of this isolator within the 4 to 22 GHz range.

V. DISCUSSION

When comparing the measured data with the simulated S-parameters in Fig. 4, we observe similar patterns for each scattering parameter. The S_{21} curves exhibit a transition to a flat response above a specific frequency, accompanied by minor ripples at higher frequencies. S_{22} generally shows poorer performance compared to S_{11}, especially at the low frequency end. They both show a gradual decrease below 12 GHz and fluctuations above that range. The S_{12} curves exhibit an initial value above −20 dB around 4 GHz, followed by a deep null near 9 GHz, after which there is a gradual increase and eventually flatten out at approximately −17 dB above 18 GHz.

As discussed in Section III, there are certain discrepancies between the simulation and measurement data due to our limited knowledge of the material properties at cryogenic temperatures in addition to other limitations of the simulations. The first discrepancy is that the simulated S_{21} curve flattens at higher frequencies, which can be attributed to the requirement of setting the magnetic bias in the ferrite substrates to full saturation during simulations. This saturation effect influences the insertion loss performance, especially at lower operating frequencies, particularly below f_m. Additionally, the measured insertion loss is lower than the simulated values due to improved dielectric loss and conduction loss at cryogenic temperatures. The magnetic field uniformity is also improved as the reduced permeability alters the demagnetization factor of the ferrite slabs at low temperatures. Secondly, both return losses (S_{11} and S_{22}) exhibit improvements in the cryogenic measurements, especially at low frequencies towards 4 GHz. In the simulations, dielectric spacers are used to isolate the excitation ports and the ferrite material. Although the spacers possess the same dielectric constant as the ferrite, there could be differences in characteristic impedance due to the magnetic properties of the ferrite substrates, resulting in impedance mismatches. Lastly, the measured isolation is weaker at lower frequencies, and we attribute this to the electromagnetic properties of the load material changing at cryogenic temperatures. Nevertheless, through multiple simulation and prototyping iterations during optimization, we have achieved measurement results that meet the design objectives.

Table 1 compares the performance of wideband edge-mode isolators presented in previous published works and currently available commercial products. The isolators operating at a cryogenic temperature of 4 K provide exceptionally low insertion loss, typically below 1.0 dB. The isolator presented in this work surpasses all previous achievements by delivering unprecedented performance over an ultra-wide frequency range of 4 to 22 GHz.

To assess the effectiveness of the new asymmetric isolator proposed in this study in comparison to the symmetric isolator from [13], cryogenic input return loss (S_{11}) measurements were conducted at a temperature of 4 K for three different setups. The first setup involved a commercial LNA manufactured by Low Noise Factory (model LNC6_20D). The second setup included the symmetric isolator placed in front of that LNA, and the final setup featured the new asymmetric

TABLE 1. Performance of Wideband Edge-Mode Isolators

Bandwidth (GHz)	Insertion Loss (dB)	Isolation (dB)	S_{11} (dB)	S_{22} (dB)	Operation Temperature (K)	References
5–15	∼2	>17 (5–12.5 GHz) >10 (12.5–15 GHz)	-	-	300	[6]
2–10 3.5–14 6–18 8–20	1.5 1 1.2 1.2	15 20 17 17	-19 -17 -17 -15	-19 -17 -17 -15	300	[8]
5–7.7	∼2.0 (5.8–6.8 GHz) <4 (5–7.7 GHz)	>20 (5–7.2 GHz) >10 (7.2–7.7 GHz)	<-20 (5–6.8 GHz) ∼-10 (6.8–7.4 GHz)	<-20 (5–6.8 GHz) ∼-10 (6.8–7.4 GHz)	300	[10]
4–12	<1.0 (4–10 GHz) ∼1.5 (10–12 GHz)	>20	<-15 (4–10 GHz) ∼-15 (10–12 GHz)	<-15 (4–10 GHz) ∼-15 (10–12 GHz)	4	Model CWJ1015KIBZFM Quinstar Technology Inc.
4–22	<1.0	>15 (4–14 GHz) > 10 (14–22 GHz)	<-20 (4–14 GHz) <-15 (14–22 GHz)	<-20 (4–14 GHz) <-15 (14–22 GHz)	4	[13]
4–22	<1.0	>20 (4–15 GHz) ∼17 (15–22 GHz)	<-20	<-15	4	This Work

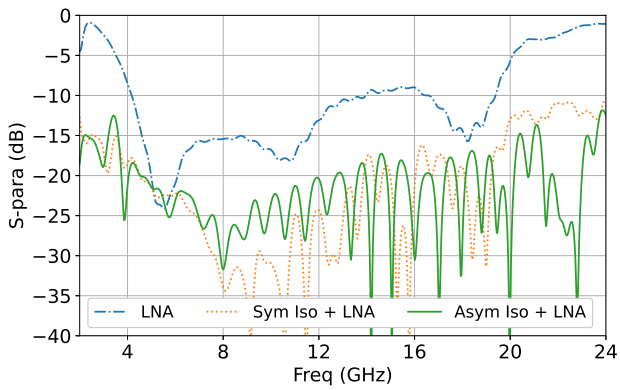

FIGURE 12. The S_{11} measured at a temperature of 4 K for three setups: a single commercial LNA (LNC6_20D from Low Noise Factory), a symmetric isolator from [13] and the same LNA, and the new asymmetric isolator and the same LNA.

isolator paired with the same LNA. The measured values of S_{11} from all three setups are plotted in Fig. 12. Referring to the figure, the S_{11} of the LNA agrees very well with the technical measurement data from the manufacturer. It exhibits poor input match, around 4 GHz and above 12 GHz. The two S_{11} plots for the isolator–LNA cascades demonstrate that both isolators effectively attenuate the reflection signal from the LNA to a level lower than −15 dB across the 4–20 GHz range. Below 14 GHz, where both isolators have good isolation performance, the symmetric isolator setup demonstrates superior return loss due to its better impedance matching at the output port (S_{22}). However, the measured S_{11} from the asymmetric isolator setup is still below −20 dB between 5 and 16 GHz, which is an acceptable level in practical terms. Above 16 GHz, the isolation of the symmetric isolator becomes poorer. As a result, the asymmetric isolator setup demonstrates better performance, except around 18 GHz where the reflection from the LNA itself is relatively low, and the isolator's return loss performance dominates. In summary, the new asymmetric isolator significantly enhanced the bandwidth performance, especially towards the higher frequency range.

VI. CONCLUSION

We have successfully developed an enhanced cryogenic wideband edge-mode isolator based on an innovative asymmetric circuit design. This isolator outperforms its predecessor by providing superior isolation performance, particularly at the high-frequency end of the band, thanks to its adaptable circuit for the reverse wave. With its remarkable performance across the frequency range 4 to 22 GHz, the implementation of this isolator will bring forth significant benefits to vital facilities in radio astronomy, including SMA and ALMA, by doubling or even tripling the instantaneous IF bandwidth of their receivers for spectral line observations and enhancing the sensitivity of dust continuum measurements.

This high performance isolator may also find applications in cryogenic RF systems. As discussed in Section II-A, this edge-mode isolator offers flexibility in adjusting its performance by altering the distance between the circuit's edge and the load absorbers, represented by w as shown in Fig. 2. Decreasing the w value results in an increase in the isolator's isolation at the cost of higher insertion loss. In our laboratory, we have successfully demonstrated single isolators with over 50 dB isolation with manageable insertion loss and bandwidth. In the field of quantum computing, the current typical bandwidth requirement is around 4 GHz. If wider bandwidth is required in the future, this isolator provides the flexibility of cascading to achieve high isolation, making it an ideal choice for such applications.

Our future plan in cryogenic isolator development will be centered around two primary objectives. Firstly, we aim to further reducing the insertion loss by utilizing low-loss materials for the circuit, such as silver or even superconducting materials. Secondly, we will continue our focus on enhancing the isolation performance by introducing new circuit geometry to further suppress the higher-order and volume modes at higher frequencies.

REFERENCES

[1] C.-Y. E. Tong, R. Blundell, K. G. Megerian, J. A. Stern, S.-K. Pan, and M. Pospieszalski, "A distributed lumped-element SIS mixer with very wide instantaneous bandwidth," *IEEE Trans. Appl. Supercond.*, vol. 15, no. 2, pp. 490–494, Jun. 2005.

[2] C.-Y. E. Tong, P. K. Grimes, A. Barbier, K. Schuster, and M.-J. Wang, "Design and performance of a 3-junction series distributed SIS mixer for wide IF applications," *IEEE Trans. Appl. Supercond.*, vol. 23, no. 3, Jun. 2013, Art. no. 1400404.

[3] C. Tong et al., "Development of SIS receivers with ultra-wide instantaneous bandwidth for wSMA," in *Proc. 29th Int. Symp. Space THz Technol.*, 2018, pp. 249–254.

[4] T. Kojima et al., "275-500-GHz widebandwaveguide SIS mixers," *IEEE Trans. THz Sci. Technol.*, vol. 8, no. 6, pp. 638–646, Nov. 2018.

[5] J. D. Garrett, C.-Y. E. Tong, L. Zeng, T.-J. Chen, and M.-J. Wang, "A 345-GHz sideband-separating receiver prototype with ultra-wide instantaneous bandwidth," *IEEE Trans. THz Sci. Technol.*, vol. 13, no. 3, pp. 237–245, May 2023.

[6] M. E. Hines, "Reciprocal and nonreciprocal modes of propagation in ferrite stripline and microstrip devices," *IEEE Trans. Microw. Theory Techn.*, vol. 19, no. 5, pp. 442–451, May 1971.

[7] L. Courtois, G. Forterre, and B. Chiron, "Improvement in broad band ferrite isolators," in *Proc. Amer. Inst. Phys. Conf. Ser.*, 1975, vol. 24, pp. 501–502.

[8] G. Forterre, B. Chiron, and L. Courtois, "A survey of broad band stripline ferrite isolators," *IEEE Trans. Magn.*, vol. 11, no. 5, pp. 1279–1281, Sep. 1975.

[9] M. Dydyk, "Edge guide: One path to wideband isolator design," *Microwave*, vol. 16, pp. 54–58, 1977.

[10] K. Araki, T. Koyama, and Y. Naito, "A new type of isolator using the edge-guided mode," *IEEE Trans. Microw. Theory Techn.*, vol. 23, no. 3, pp. 321–321, Mar. 1975.

[11] Y. Uzawa et al., "Development of the 787-950 GHz ALMA band 10 cartridge," in *Proc. 20th Int. Symp. SpaceTHz Technol.*, 2009, Art. no. 12.

[12] A. Baryshev, R. Hesper, and W. Wild, "ALMA band 9 receiver design and performance," in *IEEE MTT-S Int. Microw. Symp. Dig.*, 2015, pp. 1–5.

[13] L. Zeng, C. E. Tong, R. Blundell, P. K. Grimes, and S. N. Paine, "A low-loss edge-mode isolator with improved bandwidth for cryogenic operation," *IEEE Trans. Microw. Theory Techn.*, vol. 66, no. 5, pp. 2154–2160, May 2018.

[14] P. De Santis, "Edge-guided modes in ferrite microstrips with curved edges," *Appl. Phys.*, vol. 4, pp. 167–174, Jul. 1974.

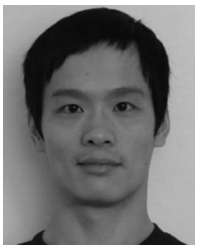

LINGZHEN ZENG received the B.S. degree from the University of Science and Technology of China, Hefei, China, in 2005, and the Ph.D. degree in astronomy from Johns Hopkins University, Baltimore, MD, USA, in 2012. Since then, he has been a Physicist with the Center for Astrophysics | Harvard & Smithsonian, Cambridge, MA, USA. His research interests include astrophysics, millimeter-wave instrumentation, and cosmology.

CHEUK-YU EDWARD TONG (Member, IEEE) received the B.S. degree in electrical engineering from the University of Hong Kong, Hong Kong, and the Ph.D. degree from the Institut de Radioastronomie Millimétrique, Grenoble, France. He was a Postdoctoral Fellow with Applied Superconductivity Research Group, Communications Research Laboratory, Tokyo, Japan, which is currently known as NICT. In the past 30 years, he has been with Smithsonian Astrophysical Observatory, Cambridge, MA, USA, where he is currently involved with the development of receivers for the Submillimeter Array, a submillimeter interferometer on Mauna Kea, Hawaii. His research interests include superconducting receivers, terahertz technology, low-noise receiver systems, and microwave measurement methods.

SCOTT N. PAINE received the B.S. degree in applied physics from the California Institute of Technology, Pasadena, CA, USA, in 1984, and the Ph.D. degree in physics from the Massachusetts Institute of Technology, Cambridge, MA, USA, in 1992. He is currently a Senior Physicist with the Radio and Geoastronomy division of the Smithsonian Astrophysical Observatory with the Center for Astrophysics | Harvard & Smithsonian, Cambridge, MA, USA. He has been affiliated with the Submillimeter Array radio interferometer on Maunakea, Hawaii, since its original development and construction, and is also active in the CMB-S4 experimental cosmology project. His research interests include advancing instrumentation and techniques for radio astronomy, experimental cosmology, and atmospheric radiometry, and measuring and modeling radiative properties of the terrestrial atmosphere with broad application to astronomy, and earth science.